Appl Phys A (2012) 109:367–376
DOI 10.1007/s00339-012-7269-8

Applied Physics A
Materials Science & Processing

Size distribution control of metal nanoparticles using femtosecond laser pulse train: a molecular dynamics simulation

Xin Li · Lan Jiang

Received: 16 June 2012 / Accepted: 10 September 2012 / Published online: 29 September 2012
© Springer-Verlag Berlin Heidelberg 2012

Abstract Microscopic mechanisms and optimization of metal nanoparticle size distribution control using femtosecond laser pulse trains are studied by molecular dynamics simulations combined with the two-temperature model. Various pulse train designs, including subpulse numbers, separations, and energy distributions are compared, which demonstrate that the minimal mean nanoparticle sizes are achieved at the maximal subpulse numbers with uniform energy distributions. Femtosecond laser pulse trains significantly alter the film thermodynamical properties, adjust the film phase change mechanisms, and hence control the nanoparticle size distributions. As subpulse numbers and separations increase, alternation of film thermodynamical properties suppresses phase explosion, favors critical point phase separation, and significantly reduces mean nanoparticle size distributions. Correspondingly, the relative ratio of two phase change mechanisms causes two distinct nanoparticle size control regimes, where phase explosion leads to strong nanoparticle size control, and increasing ratio of critical point phase separation leads to gentle nanoparticles size control.

1 Introduction

Metal nanoparticles have drawn intensive fundamental and application research attentions due to their remarkable size-dependent properties [1, 2]. For many applications, such as pulsed laser deposition, chemical and biological sensing, and magnetic information storage, the size distribution control of metal nanoparticles plays a crucial role to enhance thin film quality, sensing performance, and magnetic material properties [3–5].

Laser ablation is the most simple and efficient method for metal nanoparticles generation in both vacuum and liquid [6–9]. Amoruso et al. [8] studied femtosecond laser ablation of Au, Ag, and Ni targets in vacuum and prepared 10–50 nm nanoparticles in diameter with narrow size distributions on mica substrates. Kabashin et al. [9] investigated femtosecond laser ablation of Au targets in water and produced 3–10 nm colloidal nanoparticles with narrow size distributions. Conventionally, the size distributions of metal nanoparticles can be influenced by laser parameters such as laser wavelength, laser fluence, and pulse duration [10–13]. Amoruso et al. [10] studied the dependence on laser wavelength of Ni nanoparticles generation in vacuum and indicated that ultraviolet light helped the smaller particles with narrower size distributions as compared with visible light. Chakravarty et al. [12] explored the dependence on pulse duration of Ag nanoparticles generation in vacuum and demonstrated that femtosecond pulses typically generated smaller nanoparticles as compared with picosecond pulses. Although the size distributions of metal nanoparticles can be manipulated by laser parameters to a certain degree, its full control remains a big challenge.

Recently, it is experimentally demonstrated that size distributions of metal nanoparticles can be dramatically manipulated by two-delayed femtosecond pulses in both vacuum and liquid [14–16]. Wang et al. [14] investigated two-delayed femtosecond pulses ablation of Cu targets in vacuum by a hybrid time-gated imaging technique and demonstrated that ablation plume characteristics could be dramatically altered by the second subpulse. Noël et al. [15] ex-

X. Li · L. Jiang (✉)
NanoManufacturing Fundamental Research Joint Laboratory of National Science Foundation of China, School of Mechanical Engineering, Beijing Institute of Technology, Beijing 100081, People's Republic of China
e-mail: jianglan@bit.edu.cn
Fax: +86-10-68914517

plored two-delayed femtosecond pulses ablation of Au and Cu targets in vacuum by using fast imaging and found that the relative frequency of metal nanoparticles in ablation plumes monotonously decreased as subpulse separation increased. Axente et al. [16] studied two-delayed femtosecond pulses ablation of Au targets in ethanol solutions and discovered that the size distributions of colloidal nanoparticles were greatly influenced by the subpulse separation within a train.

Developments of optics technology have made it possible to obtain almost arbitrary pulse shapes [17]. The pulse train techniques can shape classical femtosecond pulse to femtosecond pulse train with multiple subpulses of arbitrary pulse separations or energy distributions, which may greatly influence the laser-materials interaction [18, 19] and open exciting new possibilities in full control of metal nanoparticle size distributions. It should be mentioned that two-delayed femtosecond pulse technique is one special case of pulse train techniques. The further optimal designs of pulse train techniques will play a significant role for metal nanoparticle size distribution control.

Theoretically, molecular dynamics simulations are capable of providing systematic and comprehensive information of laser ablation and corresponding nanoparticle generation [20]. Amoruso et al. [21] studied femtosecond laser ablation of Al targets at different fluencies and demonstrated that nanoparticles in ablation plumes were directly generated through phase explosion. Zhigilei et al. [22] examined ultrashort pulse laser ablation of Ni targets and demonstrated that three processes (melting, spallation, and phase explosion) occurred at the same time scale, where transition from spallation to phase explosion induced abrupt transformation of ablation plumes. The aforementioned studies explain metal nanoparticle generation by classical femtosecond pulse ablation. However, microscopic mechanisms of metal nanoparticle size distribution control with pulse train techniques are still unclear and need great efforts to be revealed.

In this paper, femtosecond laser pulse train ablation of Ni targets is studied by molecular dynamics simulations for various pulse train designs such as different sub-pulse numbers, subpulse separations, and subpulse energy distributions. The microscopic mechanisms and optimization of metal nanoparticle size distribution control with pulse train techniques are carefully investigated. It should be mentioned that the aforementioned mechanisms may be widely applicable due to similar nanoparticle formation mechanisms by femtosecond laser ablation of various metals [8].

2 Simulation method

The femtosecond laser pulse train ablation of Ni targets and corresponding nanoparticle generation are studied by a model combining molecular dynamics (MD) simulations and the two-temperature model (TTM), which has been widely used in ultrashort laser processing of metals [23–25].

In TTM, the electrons and lattices are treated as two separate subsystems, where the energy transfer processes for ultrashort laser heating of metals are described by [24]

$$C_e(T_e)\frac{\partial T_e}{\partial t} = \nabla\big(k_e(T_e)\nabla T_e\big) - G(T_e - T_l) + S(z,t) \tag{1}$$

$$C_l(T_l)\frac{\partial T_l}{\partial t} = G(T_e - T_l) \tag{2}$$

where T_e and T_l are the electron and lattice temperatures, respectively, C_e and C_l are the electron and lattice heat capacities, respectively, k_e is the electron heat conductivity, and G is the electron-lattice coupling factor. This study assumes that $C_e = \gamma T_e, \gamma = 1065\ \mathrm{J/m^3\,K^2}$, $C_l = 4.1\ \mathrm{J/kg\,K}$, $k_e = k_0 T_e/T_l, k_0 = 91\ \mathrm{W/m\,K}$, and $G = 3.6\times10^{17}\ \mathrm{W/m^3\,K}$ [26]. The femtosecond pulse trains are imposed on the Ni thin films along the z direction with subpulses of spatial uniform distributions and temporal Gaussian distributions, and the laser source term S is expressed as

$$\begin{aligned} S(z,t) = {} & \frac{0.94J}{t_p\delta}\sum_{i=1}^{N} rat_i \\ & \times \exp\left(-2.77\left(\frac{t - t_0 - (i-1)t_{\mathrm{delay}}}{t_p}\right)^2\right) \\ & \times \exp\left(-\frac{z - z_{i0}}{\delta}\right) \end{aligned} \tag{3}$$

where J is the absorbed fluence of femtosecond pulse trains, t_p is the pulse duration of subpulses, t_0 is the center of the first subpulse, z_{i0} is the position of dynamic surface position during the ith subpulse irradiation, δ is the optical penetration depth, N is the subpulse number, t_{delay} is the subpulse separation, rat_i is the fluence ratio of the ith sub-pulses, and t is the time. This study assumes that $J = 0.32\ \mathrm{J/cm^2}$, $t_p = 100$ fs, and $\delta = 13.5$ nm [26].

In MD simulations, the Ni targets have a thickness of 70 nm (in the z direction) and lateral dimensions of 40 nm × 2 nm (in the x and y directions), consisting of about 534,000 atoms. The interactions among Ni atoms are described by the Morse potential [27]

$$\Phi(r_{ij}) = D\big(e^{-2\alpha(r_{ij}-r_0)} - 2e^{-\alpha(r_{ij}-r_0)}\big) \tag{4}$$

where D is the total dissociation energy, α is a constant with dimension of reciprocal distance, and r_0 is an equilibrium distance. This study assumes $D = 0.4205$ eV, $\alpha = 14.199\ \mathrm{nm^{-1}}$, and $r_0 = 0.278$ nm. Free boundary condition and nonreflecting boundary condition are applied in the z direction, and periodical boundary conditions are applied in the x and y directions [24].

In the combined model (TTM + MD), the energy transfer processes should also be described by thermal transport equations of TTM, and MD simulations are introduced. As MD simulations cannot describe the energy transfer by electrons, the thermal transport equation for electrons (Eq. (1)) is adopted to describe the electron heating by ultrashort laser pulse. As MD simulations can describe the lattice energy transfer well, where the positions and velocities of atoms (instead of lattice temperature T_l) are used to describe the Ni targets systems, the thermal transport equation for lattices (Eq. (2)) should be substituted by another equation which includes the information of positions or velocities of atoms (Appendix). The lattice heating by the hot electrons is achieved by scaling the atom velocities with a factor β [28]:

$$\beta = \left[1 + \frac{\Delta t G(T_e - T_l)V}{0.5\sum_{i=1}^{N} m_i[(v_{xi,t} - \overline{v_{x,t}})^2 + (v_{yi,t} - \overline{v_{y,t}})^2 + (v_{zi,t} - \overline{v_{z,t}})^2]}\right]^{1/2} \tag{5}$$

where $v_{xi,t}$, $v_{yi,t}$, and $v_{zi,t}$ are the velocities of atom i in the directions x, y, and z, respectively, $\overline{v_{x,t}}$, $\overline{v_{y,t}}$, and $\overline{v_{z,t}}$ are the average velocities of atom i in the directions x, y, and z, respectively, N is the number of atoms within a sample layer, V is the volume of the layer, and Δt is the time step.

3 Results and discussion

A classical femtosecond pulse consists of "bursts" at a time separation of a few microseconds to milliseconds. A femtosecond pulse train further splits the "burst" to multiple subpulses with a femtosecond-to-picosecond time delay with arbitrary energy distributions. In this paper, various pulse train designs at the same total absorbed fluence are studied to explore the laws and mechanisms of metal nanoparticle size distribution control: (a) femtosecond pulse trains as functions of subpulse numbers, where subpulse numbers = range (1–40), subpulse separations = 1 ps, uniform energy distributions, (b) femtosecond pulse trains as functions of subpulse separations, where subpulse numbers = 2, subpulse separations = range (0–20 ps), uniform energy distributions, (c) femtosecond pulse trains as functions of subpulse energy distributions, where subpulse numbers = 2, subpulse separations = 20 ps, first subpulse fluence ratios = range (0–1), as shown in Fig. 1.

Figure 2 shows the mean particle sizes of Ni nanoparticles generated by femtosecond pulse trains. In pulse train designs of case (a), the mean nanoparticles sizes in diameters dramatically decrease as subpulse numbers increase (Fig. 2a). Two distinct different regimes are observed: (1) when subpulse numbers increase from 1 to 5, the mean nanoparticle sizes decrease sharply from 4.9 nm to 2.6 nm, which indicates strong size control effects; (2) when subpulse numbers increase from 5 to 40, the mean nanoparticles sizes further decrease slowly from 2.6 nm to 2.1 nm, which indicates gentle size control effects. In pulse train designs of case (b), the mean nanoparticle sizes in diameters remarkably decrease as subpulse separations increase (Fig. 2b), which corresponds with the experimental results of colloidal nanoparticle generation by two-delayed femtosecond pulses [15]. Similarly, strong and gentle size control regimes are observed. In pulse train designs of case (c), the mean nanoparticles sizes in diameters slightly vary as the first subpulse fluence ratios increase, where the minimum is achieved at uniform subpulse energy distributions (Fig. 2c). The simulation results demonstrate that pulse train designs play a significant role for nanoparticle size control. Among various pulse train designs, the minimal mean nanoparticle size is achieved at the maximal subpulse numbers with uniform energy distributions.

To reveal the microscopic mechanisms of metal nanoparticle size distribution control, various pulse train ablation processes of Ni targets are carefully investigated. Figure 3 shows the snapshots and particle size distributions for the

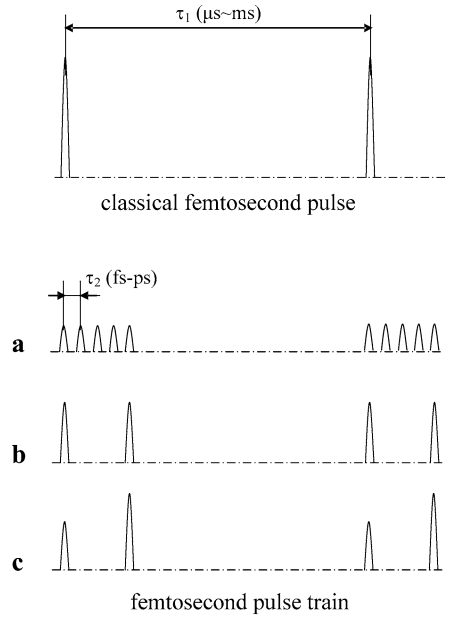

Fig. 1 Schemes of classical femtosecond pulse and femtosecond pulse train

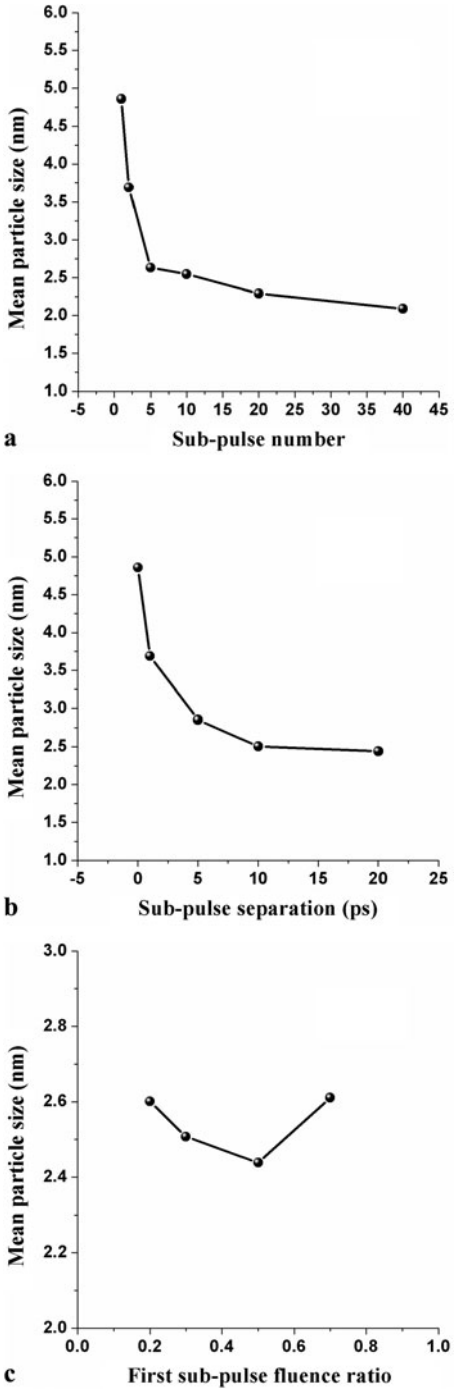

Fig. 2 Mean particle sizes of Ni nanoparticles generated at femtosecond pulse trains as functions of: (**a**) subpulse numbers (subpulse separation is 1 ps), (**b**) subpulse separations (subpulse number is 2), (**c**) first subpulse fluence ratios (subpulse number is 2), where total absorbed fluence is 0.32 J/cm^2

femtosecond pulse train as functions of subpulse numbers per train. When the subpulse number is 1 (classical femtosecond pulse), the Ni target experiences rapid melting, vapor phases appearance, gas bubbles formation inside, and film disintegration into pieces after pulse irradiation (Fig. 3a). Accompanied with film disintegration, fewer nanoparticles with larger mean size (4.9 nm in diameters) and broader distributions (0.5–10 nm in diameters) are generated (Fig. 3d). As the subpulse numbers increase, the melting front propagation velocities become slower, and gas bubbles become fewer, smaller, and finally extinct (Fig. 3b). And nanoparticle mean sizes and distributions dramatically decrease (Fig. 3e). When the subpulse number is 40 (femtosecond pulse train with 40 subpulses), the Ni target experiences slow melting, vapor phases appearance, particles/atoms spurting out, and film decomposition from film surface during pulse train irradiation (Fig. 3c). Accompanied with film decomposition, more nanoparticles with smaller mean size (2.1 nm in diameters) and narrower distributions (0.5–4 nm in diameters) are generated (Fig. 3f).

Table 1 Mean particle sizes and film thermodynamical properties for femtosecond pulse trains as function of subpulse numbers, where T_{max} is the maximal lattice temperatures of film surfaces, σ_{maxc} is the maximal film compressive stresses, σ_{maxt} is the maximal film tensile stresses, the total absorbed fluence is 0.32 J/cm^2, the subpulse separation is 1 ps

Sub-pulse number	Mean particle sizes	T_{max}	σ_{maxc}	σ_{maxt}
1	4.9 nm	9045.8 K	31.8 GPa	−7.7 GPa
2	3.7 nm	9419.9 K	30.9 GPa	−7.2 GPa
5	2.6 nm	9920.0 K	28.2 GPa	−6.6 GPa
10	2.5 nm	10245.5 K	23.7 GPa	−5.3 GPa
20	2.3 nm	10671.8 K	15.4 GPa	−3.8 GPa
40	2.1 nm	10911.5 K	10.1 GPa	−2.9 GPa

As the subpulse numbers increase at the same total absorbed fluence, the heat transfer processes are significantly changed. The increase of subpulses causes the film surfaces continuously heated, which induces a significant decrease of electron thermal conductivity and an increase in absorbed energy deposited within film surfaces. Hence, the film thermodynamical properties are significantly altered (Table 1): (1) the maximal lattice temperatures of film surfaces are gradually increased from 9045.8 K to 10911.5 K (across the critical temperature of 9450 K), which favors the critical point phase separation; (2) the maximal film compressive stresses are notably reduced from 31.8 GPa to 10.1 GPa; (3) the maximal film tensile stresses are notably reduced from −7.7 GPa to −2.9 GPa, which suppress the phase explosion, because strong tensile stresses tend to induce liquid–vapor phase separation [23]. It should be mentioned that the more subpulse numbers, the more absorbed energy deposited within film surfaces and less compressive/tensile stresses generated, which explains why the minimal mean nanoparticle size is achieved at maximal subpulse numbers.

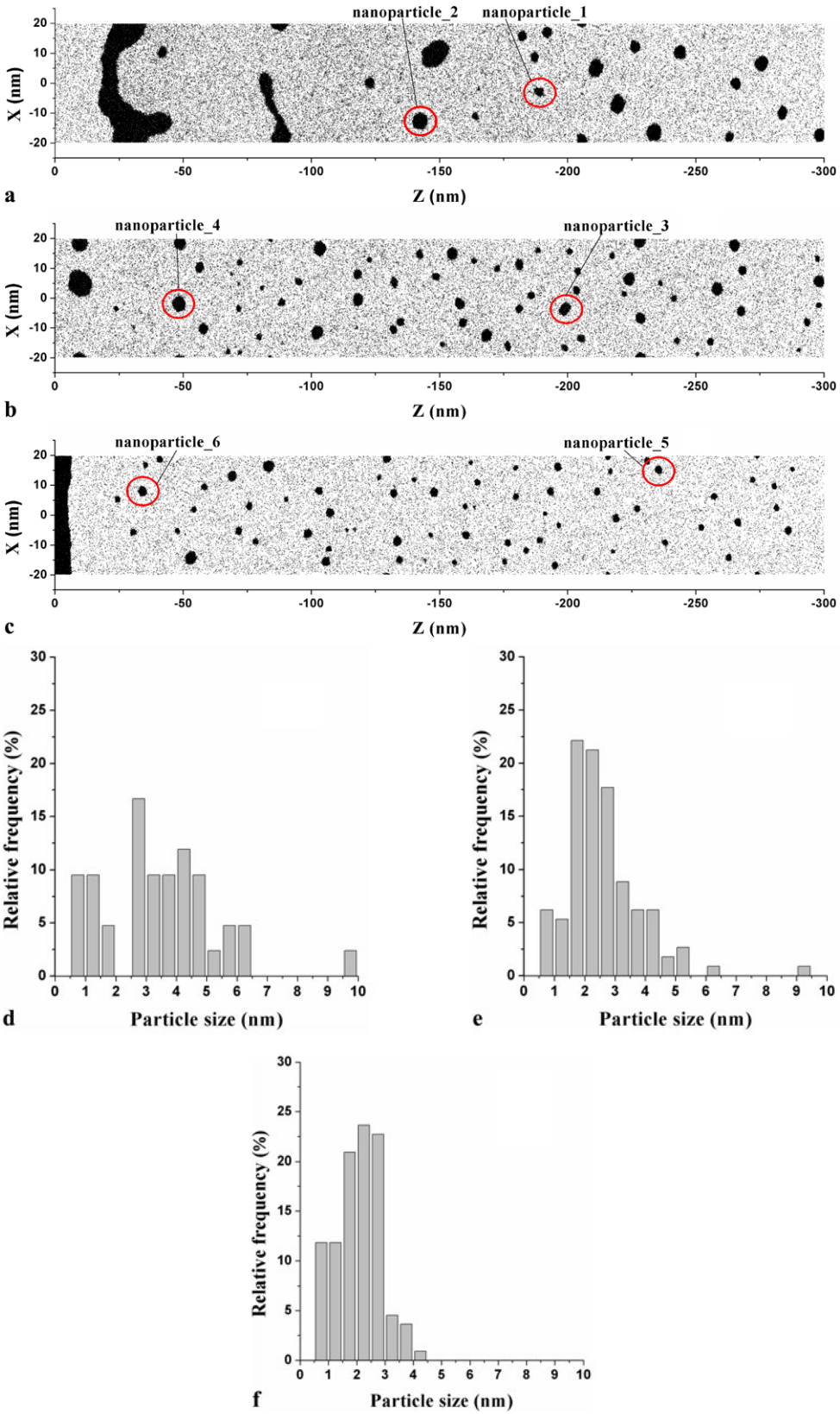

Fig. 3 The snapshots and particle size distributions of Ni nanoparticles generated at a classical femtosecond pulse [(**a**) and (**d**)], a femtosecond pulse train with 5 subpulses [(**b**) and (**e**)] and a femtosecond pulse train with 40 subpulses [(**c**) and (**f**)], where total absorbed fluence is 0.32 J/cm^2, subpulse separation is 1 ps and $t = 200$ ps

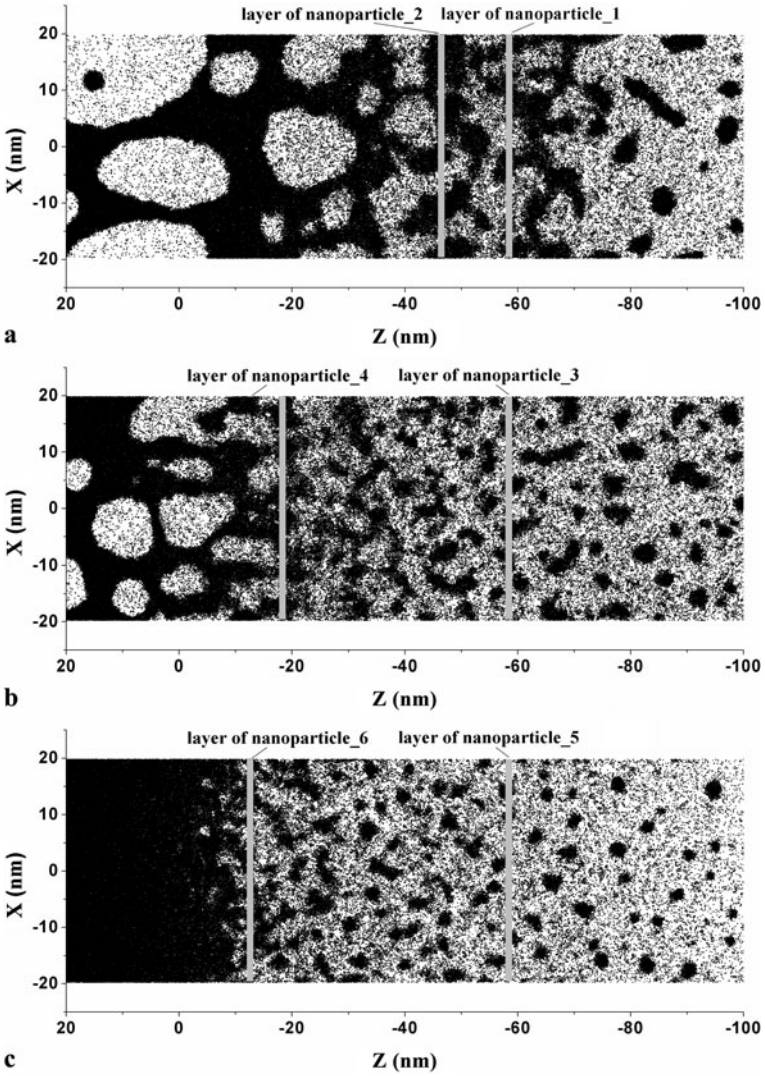

Fig. 4 The snapshots of initial nanoparticles formation and thermodynamical trajectories of marked nanoparticles in Fig. 3 for a classical femtosecond pulse [(**a**) and (**d**)], a femtosecond pulse train with 5 subpulses [(**b**) and (**e**)], and a femtosecond pulse train with 40 subpulses [(**c**) and (**f**)], where total absorbed fluence is 0.32 J/cm^2, sub-pulse separation is 1 ps and $t = 80$ ps

The pulse train ablation processes of Ni targets directly determine nanoparticle generation, where several representative nanoparticles are carefully tracked (Fig. 3 and Fig. 4). Figure 4 shows the snapshots of initial nanoparticle formation and thermodynamical trajectories of marked nanoparticles for femtosecond pulse trains as functions of subpulse numbers per train. When the subpulse number is 1, the initial nanoparticle formation is due to evolution of the small gas bubbles inside film (Fig. 4a). Initially, nanoparticles 1 and 2 are in condensed states. Thereafter, they expand rapidly with thermodynamical trajectories across metastable zones (between binodal and spinodal lines) (Fig. 4d), where phase explosion dominates nanoparticles formation. When the subpulse number is 40, the initial nanoparticles formation is due to the evolution of nanoparticles spurting out from film surface (Fig. 4c). Initially, nanoparticles 5 and 6 are in condensed states. Thereafter, nanoparticle 5 expands rapidly with thermodynamical trajectories to achieve supercritical states (Fig. 4f), where critical point phase separation dominates nanoparticle formation. However, phase explosion still dominates formation of nanoparticle 6.

As subpulse numbers increase at the same total absorbed fluence, the nanoparticles generation mechanisms are significantly influenced (Table 2). Two distinct different regimes are observed, which corresponds with the strong and gentle size control regimes. (1) When subpulse numbers increase from 1 to 5, all the nanoparticles are generated from phase explosion. Femtosecond pulse trains are highly effective for size control of nanoparticle generation from phase explosion mechanism, which leads to strong nanoparticle size control. (2) When subpulse numbers increase from 5 to 40, the nanoparticles generated from phase explosion and critical point phase separation, where the ratio of nanoparticles generated from critical point phase separation promi-

Fig. 4 (*Continued*)

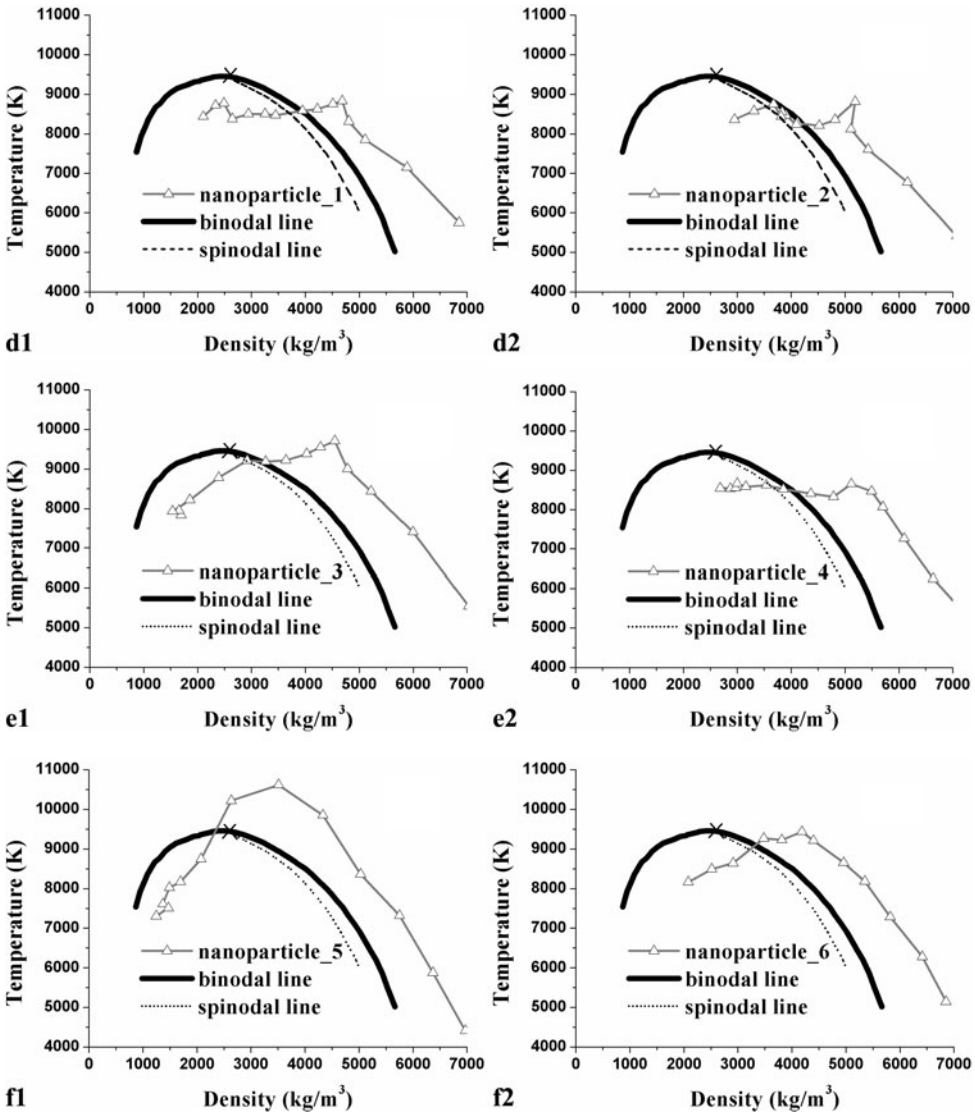

Table 2 The ratio of two phase change mechanisms (phase explosion and critical point phase separation) for Ni nanoparticles generated at femtosecond pulse trains as functions of the subpulse number, where the total absorbed fluence is 0.32 J/cm^2, the subpulse separation is 1 ps

Phase change	Sub-pulse number					
	1	2	5	10	20	40
Phase explosion	100 %	100 %	100 %	85 %	55 %	46 %
Critical point phase separation	0	0	0	15 %	45 %	54 %

Table 3 Mean particle sizes and film thermodynamical properties for femtosecond pulse trains as functions of subpulse separations, where T_{max} is the maximal lattice temperature of film surfaces, σ_{maxc} is the maximal film compressive stress, σ_{maxt} is the maximal film tensile stress, total absorbed fluence is 0.32 J/cm^2, the subpulse number is 2

Sub-pulse separation	Mean particle sizes	T_{max}	σ_{maxc}	σ_{maxt}
0	4.9 nm	9045.8 K	31.8 GPa	−7.7 GPa
1	3.7 nm	9419.9 K	30.9 GPa	−7.2 GPa
5	2.9 nm	9674.5 K	24.0 GPa	−6.6 GPa
10	2.5 nm	10063.9 K	19.2 GPa	−5.1 GPa
20	2.4 nm	9803.7 K	18.6 GPa	−3.8 GPa

nently increases from 0 % to 54 %. Femtosecond pulse trains are limitedly effective for nanoparticle generation from critical point phase separation mechanism, which leads to gentle nanoparticle size control.

For femtosecond pulse trains as functions of subpulse separations and subpulse energy distributions, similar mechanisms of metal nanoparticle size distribution control are observed. (1) As subpulse separations increase, film thermodynamical properties are significantly altered with max-

Table 4 Mean particle sizes and film thermodynamical properties for femtosecond pulse trains as functions of first subpulse fluence ratios, where T_{max} is the maximal lattice temperature of film surfaces, σ_{maxc} is the maximal film compressive stress, σ_{maxt} is the maximal film tensile stress, the total absorbed fluence is 0.32 J/cm^2, the subpulse number is 2

First sub-pulse fluence ratio	Mean particle sizes	T_{max}	σ_{maxc}	σ_{maxt}
0.2	2.6 nm	10070.3 K	28.5 GPa	−4.8 GPa
0.3	2.5 nm	10067.2 K	18.7 GPa	−4.0 GPa
0.5	2.4 nm	9803.7 K	18.6 GPa	−3.8 GPa
0.7	2.6 nm	9616.7 K	24.5 GPa	−6.1 GPa

imal lattice temperatures of film surfaces increasing to a peak value and then decreasing, and maximal film compressive/tensile stresses decreasing (Table 3), which suppress the phase explosion, favor the critical point phase separation, and induce significant decrease of mean nanoparticles sizes. (2) As the first subpulse fluence ratios increase, film thermodynamical properties are moderately varied with the maximal lattice temperatures of film surfaces decreasing and maximal film compressive/tensile stresses minimizing at uniform subpulse energy distributions (Table 4), which induce mean nanoparticle sizes slightly vary. The simulation results indicate that film compressive/tensile stresses play more important roles than lattice temperatures of film surfaces for metal nanoparticle size distribution control using femtosecond pulse trains.

4 Conclusions

MD simulations combined with TTM are employed for microscopic mechanisms and optimization of metal nanoparticle size distribution control with femtosecond laser pulse trains. The minimal mean nanoparticle sizes are achieved at the maximal subpulse numbers with uniform energy distributions. At the same total absorbed fluence, as subpulse numbers increase, increasing subpulses cause film surfaces continuously heated, which induce a significant increase in absorbed energy deposited within film surfaces. Accordingly, film thermodynamical properties are significantly altered: lattice temperatures of film surfaces increase and film compressive/tensile stresses decrease. This suppresses the phase explosion, favors the critical point phase separation, and significantly reduces mean nanoparticle sizes and narrows size distributions. Two distinct different regimes are observed for nanoparticles generation: (1) in strong size control regimes, phase explosion dominates nanoparticle generation, where femtosecond laser pulse trains are highly effective for nanoparticle size control; (2) in gentle size control regimes, phase explosion and critical point phase separation dominate nanoparticle generation (nanoparticle generation from critical point phase separation represents an increasing portion from 0 % to 54 %), where femtosecond laser pulse trains are limitedly effective for nanoparticles size control. As subpulse separations increase, film thermodynamical properties are significantly altered: lattice temperatures of film surfaces increase to a peak value and then decrease, and film compressive/tensile stresses decrease, which significantly reduces mean nanoparticle sizes and narrows size distributions. As the first subpulse fluence ratios increase, film thermodynamical properties are moderately varied: the lattice temperatures of film surfaces decrease, and film compressive/tensile stresses minimize at subpulse uniform energy distributions, which induces slight variation of mean nanoparticle sizes. Film compressive/tensile stresses play more important roles than lattice temperatures of film surfaces for metal nanoparticle size distribution control using femtosecond laser pulse trains.

Acknowledgements This work was supported by the National Natural Science Foundation of China (Grant No. 51105037 and 90923039) and Supported by Research Fund for the Doctoral Program of Higher Education (Grant No. 20111101120010).

Appendix: Scaling factor

Initially, the electron and lattice temperatures are both 300 K. The electron temperature of the next time step can be obtained by Eq. (1), which considers electron heating by ultrashort laser. The energy exchange between the electrons and lattices within the time step and finite difference layer is estimated by

$$\Delta E_{\text{exchange}} = \Delta t G (T_e - T_l) V \tag{6}$$

where Δt is the time step, and V is the volume of a sample layer. The energy exchange leads to increase of the kinetic energy of the layer. The kinetic energy of the layer is

$$E_{k,t} = 0.5 \sum_{i=1}^{N} m_i \left[(v_{xi,t} - \overline{v_{x,t}})^2 + (v_{yi,t} - \overline{v_{y,t}})^2 + (v_{zi,t} - \overline{v_{z,t}})^2 \right] \tag{7}$$

where $v_{xi,t}$, $v_{yi,t}$, and $v_{zi,t}$ are the velocities of atom i in the directions x, y, and z, respectively, and $\overline{v_{x,t}}$, $\overline{v_{y,t}}$, and $\overline{v_{z,t}}$ are the average velocities of atom i in the directions x, y, and z, respectively.

The lattice temperature T_l is related to the kinetic energy of the layer by

$$T_{l,t} = \frac{2}{3Nk_B} E_{k,t} = \frac{2}{3Nk_B} \left\{ \sum_{i=1}^{N} m_i \left[(v_{xi,t} - \overline{v_{x,t}})^2 + (v_{yi,t} - \overline{v_{y,t}})^2 + (v_{zi,t} - \overline{v_{z,t}})^2 \right] \right\} \quad (8)$$

where N is the number of atoms within the layer, and k_B is the Boltzmann constant. Hence,

$$\frac{T_{l,t+\Delta t} - T_{l,t}}{T_{l,t}} = \frac{E_{k,t+\Delta t} - E_{k,t}}{E_{k,t}} = \frac{\Delta E_{\text{exchange}}}{E_{k,t}} \quad (9)$$

where t is the time. Therefore,

$$\frac{T_{l,t+\Delta t}}{T_{l,t}} = 1 + \frac{\Delta t G(T_e - T_l)V}{0.5 \sum_{i=1}^{N} m_i [(v_{xi,t} - \overline{v_{x,t}})^2 + (v_{yi,t} - \overline{v_{y,t}})^2 + (v_{zi,t} - \overline{v_{z,t}})^2]} \quad (10)$$

According to Eq. (8) (the relation between the lattice temperature T_l and velocities of atoms) and Eq. (10), the energy exchange $\Delta t G(T_e - T_l)V$ is transferred to lattices by scaling the atom velocities with a factor β (Eq. (11)), which is equivalent to lattice energy increase by Eq. (2).

$$\beta = \frac{v_{xi,t+\Delta t}}{v_{xi,t}} = \frac{v_{yi,t+\Delta t}}{v_{yi,t}} = \frac{v_{zi,t+\Delta t}}{v_{zi,t}} = \left[1 + \frac{\Delta t G(T_e - T_l)V}{0.5 \sum_{i=1}^{N} m_i [(v_{xi,t} - \overline{v_{x,t}})^2 + (v_{yi,t} - \overline{v_{y,t}})^2 + (v_{zi,t} - \overline{v_{z,t}})^2]} \right]^{1/2} \quad (11)$$

References

1. K.L. Kelly, E. Coronado, L.L. Zhao, G.C. Schatz, The optical properties of metal nanoparticles: the influence of size, shape, and dielectric environment. J. Phys. Chem. B **107**, 668 (2003)
2. M.J. Martinez-Perez, R. de Miguel, C. Carbonera, M. Martinez-Julvez, A. Lostao, C. Piquer, C. Gomez-Moreno, J. Bartolome, F. Luis, Size-dependent properties of magnetoferritin. Nanotechnology **21**, 465707 (2010)
3. J.C. Alonso, R. Diamant, P. Castillo, M.C. Acosta-Garcia, N. Batina, E. Haro-Poniatowski, Thin films of silver nanoparticles deposited in vacuum by pulsed laser ablation using a YAG:Nd laser. Appl. Surf. Sci. **255**, 4933 (2009)
4. H. Jans, Q. Huo, Gold nanoparticle-enabled biological and chemical detection and analysis. Chem. Soc. Rev. **41**, 2849 (2012)
5. B. Liu, Z. Hu, Y. Che, Y. Chen, X. Pan, Nanoparticle generation in ultrafast pulsed laser ablation of nickel. Appl. Phys. Lett. **90**, 044103 (2007)
6. T. Nakamura, H. Magara, Y. Herbani, S. Sato, Fabrication of silver nanoparticles by highly intense laser irradiation of aqueous solution. Appl. Phys. A **104**, 1021 (2011)
7. P.M. Ossi, F. Neri, N. Santo, S. Trusso, Noble metal nanoparticles produced by nanosecond laser ablation. Appl. Phys. A **104**, 829 (2011)
8. S. Amoruso, G. Ausanio, R. Bruzzese, M. Vitiello, X. Wang, Femtosecond laser pulse irradiation of solid targets as a general route to nanoparticle formation in a vacuum. Phys. Rev. B **71**, 033406 (2005)
9. A.V. Kabashin, M. Meunier, Synthesis of colloidal nanoparticles during femtosecond laser ablation of gold in water. J. Appl. Phys. **94**, 7941 (2003)
10. S. Amoruso, R. Bruzzese, X. Wang, N.N. Nedialkov, P.A. Atanasov, An analysis of the dependence on photon energy of the process of nanoparticle generation by femtosecond laser ablation in a vacuum. Nanotechnology **18**, 145612 (2007)
11. E. Akman, B.G. Oztoprak, M. Gunes, E. Kacar, A. Demir, Effect of femtosecond Ti:sapphire laser wavelengths on plasmonic behaviour and size evolution of silver nanoparticles. Photonics Nanostruct. **9**, 276 (2011)
12. U. Chakravarty, P.A. Naik, C. Mukherjee, S.R. Kumbhare, P.D. Gupta, Formation of metal nanoparticles of various sizes in plasma plumes produced by Ti:sapphire laser pulses. J. Appl. Phys. **108**, 053107 (2010)
13. D. Riabinina, M. Chaker, J. Margot, Dependence of gold nanoparticle production on pulse duration by laser ablation in liquid media. Nanotechnology **23**, 135603 (2012)
14. X. Wang, S. Amoruso, J. Xia, Temporally and spectrally resolved analysis of a copper plasma plume produced by ultrafast laser ablation. Appl. Surf. Sci. **255**, 5211 (2009)
15. S. Noël, J. Hermann, Reducing nanoparticles in metal ablation plumes produced by two delayed short laser pulses. Appl. Phys. Lett. **94**, 053120 (2009)
16. E. Axente, M. Barberoglou, P.G. Kuzmin, E. Magoulakis, P.A. Loukakos, E. Stratakis, G.A. Shafeev, C. Fotakis, Size distribution of Au NPs generated by laser ablation of a gold target in liquid with time-delayed femtosecond pulses (2010). arXiv:1008.0374
17. L. Jiang, H.L. Tsai, Repeatable nanostructures in dielectrics by femtosecond laser pulse trains. Appl. Phys. Lett. **87**, 151104 (2005)
18. Z. Hu, S. Singha, R.J. Gordon, Controlling the photoluminescence of gallium arsenide with trains of ultrashort laser pulses. Phys. Rev. B **82**, 115204 (2010)
19. M. Guillermin, C. Liebig, F. Garrelie, R. Stoian, A.S. Loir, E. Audouard, Adaptive control of femtosecond laser ablation plasma emission. Appl. Surf. Sci. **255**, 5163 (2009)
20. X. Wang, X. Xu, Nanoparticles formed in picosecond laser argon crystal interaction. J. Heat Transf. **125**, 1147 (2002)
21. S. Amoruso, R. Bruzzese, M. Vitiello, N.N. Nedialkov, P.A. Atanasov, Experimental and theoretical investigations of femtosecond laser ablation of aluminum in vacuum. J. Appl. Phys. **98**, 044907 (2005)
22. L.V. Zhigilei, Z. Lin, D.S. Ivanov, Atomistic modeling of short pulse laser ablation of metals: connections between melting, spallation, and phase explosion. J. Phys. Chem. C **113**, 11892 (2009)

23. X. Li, L. Jiang, H.L. Tsai, Phase change mechanisms during femtosecond laser pulse train ablation of nickel thin films. J. Appl. Phys. **106**, 064906 (2009)
24. C. Cheng, X. Xu, Mechanisms of decomposition of metal during femtosecond laser ablation. Phys. Rev. B **72**, 165415 (2005)
25. D.S. Ivanov, L.V. Zhigilei, Combined atomistic-continuum modeling of short-pulse laser melting and disintegration of metal films. Phys. Rev. B **68**, 064114 (2003)
26. J. Hohlfeld, S.S. Wellershoff, J. Gudde, U. Conrad, V. Jahnke, E. Matthias, Electron and lattice dynamics following optical excitation of metals. Chem. Phys. **251**, 237 (2000)
27. L.A. Girifalco, V.G. Weizer, Application of the morse potential function to cubic metals. Phys. Rev. **114**, 687 (1959)
28. X. Wang, Thermal and thermomechanical phenomena in picosecond laser copper interaction. J. Heat Transf. **126**, 355 (2004)